The structure of gravity currents propagating in finite domains

Nuno Filipe Grenho Silvestre Instituto Superior Técnico

Abstract

Gravity currents are primarily horizontal flows driven by density differences between two or more contacting fluids which can be found in both natural and man-made environments. These currents have been widely studied since the second half of the XX century. However, most of the contributions have focused on the role of the density imbalance, and only recently some works have drawn attention to other factors such as the bed roughness.

The main goal of this work is to analyse the effect of complex geometries and different roughness beds in the propagation of gravity currents through laboratory experiments. These comprised a point and continuous release of a *NaCl* solution ($\rho_c = 1.027$ g.cm^{-3}) into a tank with resting freshwater ($\rho_a = 0.999$ g.cm^{-3}). The transport and mixing processes were assessed through image analysis techniques and Particle Image Velocimetry was employed in the study of the velocity fields.

The results showed that geometry constraints induce flow patterns that generate complex reflection waves which in turn interact with the structures at the current's front. They are also responsible for recirculation flows and zones of lower dilution. Regarding the effects of bed roughness, it can be observed a decrease in the propagation velocity in which the flow of dense fluid between the voids on the bed seems to be an important mechanism for that loss of momentum. It also induces more fragmented instability structures at the current's front.

Keywords: Gravity Currents, Geometry Effects, Bed Roughness, Image Analysis Techniques, Particle Image Velocimetry

1. Introduction

A gravity current is the primarily horizontal flow driven by the difference in specific weight between two or more contacting fluids. That heterogeneity may be due to chemical composition, temperature gradients, dissolved substances, particles in suspension or a combination of these. A wide range of gravity currents can be observed in both natural and human-made environments, from large-scale geophysical flows to small industrial applications (Simpson, 1997).

In the atmosphere, sea-breeze fronts and katabatic winds are well-known examples of gravity currents. For instance, these latter play a major role in the formation of the so-called cold air pools that result from the accumulation of high-density air in constraining topography. Several impacts can be mentioned, namely the possibility of frost damage in agricultural fields and the effects on the performance of aircrafts flying through them. Examples in the atmosphere also include particle-laden gravity currents such as avalanches, pyroclastic flows and dust storms which can reach hundreds of metres in elevation and often travel at tens of metres per second (Doronzo *et al.*, 2016).

Regarding water masses, large-scale examples include the global ocean circulation which plays a key role in the maintenance of Earth's climate and the Mediterranean outflow at Strait of Gibraltar. This latter is particularly interest as it takes place through a constraining topography which generates very important internal processes (Morozov *et al.*, 2002). Likewise, particle-laden currents are also present in the water masses and are commonly known as turbidity currents. For example, they can be observed in rivers and lakes, resulting from the high concentration of sediments during floods and after intense rainfall. When entering the receiving water basins, the flow velocity decrease induces the sedimentation of those particles leading to problems of loss of storage capacity in reservoirs and outlets/intakes clogging which have been a major subject in the research of the sustainable use of such infrastructures (Cesare *et al.*, 2001, Oehy and Schleiss, 2007).

Nonetheless, gravity currents are also caused by human activities with examples including oil spillage, the discharge of cooling waters used in power plants and outflows from wastewater treatment plants. In this later case, the density currents are mainly due to the presence of suspended material that might have sorbed different substances and which can be harmful to the ecosystems. Moreover, these flows are typically present in shallow river's lower courses where several infrastructures are built (e.g., ports and outfalls). Hence, the study and prediction of these currents' propagation is critical for complete assessment of the environmental exposure to pollutants carried by them and it must be supported by further investigation on the interaction between these flows and the surrounding elements (Kneller and Buckee, 2000, Theiler and Franca, 2016). However, most of the works in gravity currents has been focused on the propagation due to the density gradient and only few studies have drawn attention to the influence of the surrounding constraints.

2. Literature review

2.1. Anatomy of a gravity current

Gravity currents can occur with both liquids and gases that are in motion or quiescent. Despite their anatomy can be described in broad detail, it is not possible to define a universal profile since it is particularly complex and it depends on several physical factors (Simpson, 1982). The basic shape has been discussed in many studies and typically two regions can be identified. At the leading edge, a sharp dividing interface between the two fluids is formed, exhibiting the so-called head. This front advances into the ambient fluid and it is followed by the body of the current which is never deeper than the former. The head and body regions are identified in the sketch of a typical gravity current presented in Figure 1.

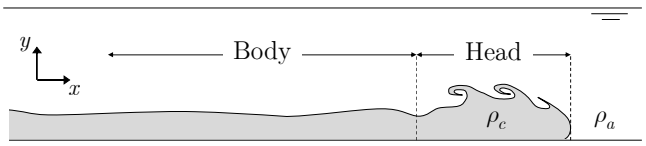

Figure 1 - The general shape of a gravity current of density ρ_c propagating in a less dense ambient fluid of density ρ_a.

The frontal zone is characterized by a three-dimensional unsteady flow that results from shear and gravitational instabilities, Kelvin-Helmholtz billows and a complex shifting pattern of lobes and clefts, respectively (Simpson, 1969, 1972). Lobes and clefts are formed when the less dense ambient fluid is over-ridden by the current propagating along a no-slip lower boundary. Using a shadowgraph technique, Simpson (1972) has traced the time-evolution of their formation as shown in Figure 2 and it can be observed that clefts can appear but never vanish, being continually absorbed by neighbours.

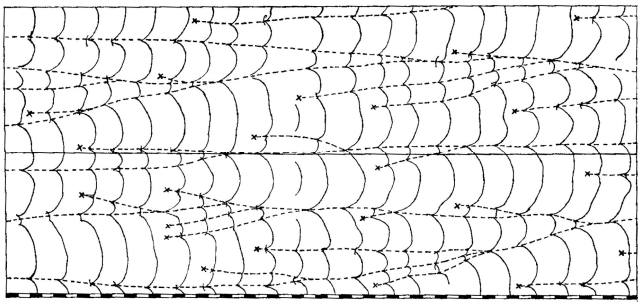

Figure 2 - Time-evolution of lobes drawn from shadowgraph series (from Simpson, 1972).

On the other hand, Kelvin-Helmholtz billows are, in basic form, rolls of fluid along the density interface where the opposite movement induces the velocity shear. These remain quasi-steady in the current body, fading away due to continuous entrainment of ambient fluid.

2.2. The study of gravity currents

Gravity currents have been widely studied through both experimental and theoretical works since the second half of the XX century. In what concerns experimental research, most of the effort has been directed towards understanding these flows in rectangular tanks, typically with homogeneous ambient fluids that are initially at rest, or with a simple prescribed motion (Simpson, 1997). The lock-exchange is a well-known technique that consists of the sudden removal of a gate causing the release of a fixed volume of dense fluid into another of less density. Usually, three distinct phases can be observed: (1) the "slumping phase" during which the current develops at a constant speed and the head is formed, followed by (2) the self-similar phase governed by a buoyancy-inertia balance and (3) a final phase in which viscous effects become relevant. Since extensive research has been carried out over the years, the general dynamics of these flows are now thought to be well understood.

In turn, the typical structure of gravity currents obtained with continuous releases denotes a steady flow in the body region. Therefore, they are usually performed to characterize the mean structure of the current in terms of density, velocity and turbulence (Martin and García, 2009, Stagnaro and Pittaluga, 2014) and to study mixing processes and entrainment (Ellison and Turner, 1959, Parker *et al.*, 1987, Cenedese and Adduce, 2010).

Definition of current depth

Despite the extensive research carried out since the 1950s, the definition for the depth of a gravity current remains an open question (Stacey and Bowen, 1988, Buckee *et al.*, 2001, Shin *et al.*, 2004). The most common approach is to evaluate the depth as the height on which the excess density and velocity are approximated to be constant along the upward-normal to the bed, z, and respectively equal to the fractional depth-averaged excess density (F_e) and velocity (U). This definition corresponds to the solution of the following system:

$$\begin{cases} q = UH = \int_0^\infty u dz \\ U^2 H = \int_0^\infty u^2 dz \\ U F_e H = \int_0^\infty u f_e dz \end{cases} \quad (1)$$

where q is the unit width discharge of the current, u is the stream-wise flow velocity and f_e is the fractional excess density. Besides it is not necessarily physical meaningful, the computing of the integrals presented above (Expression 1) requires a finite value to the upper limit of the integration. Therefore, since different criteria have been applied to define that limit, the current depth definition remains ambiguous.

Bed roughness effects

Most of the investigation efforts deal with flows developing over smooth beds and only lately attention has been drawn to the dynamics of gravity currents propagating over rough beds (Peters and Venart, 1999, Batt, 2008, La Rocca *et al.*, 2008, Sequeiros *et al.*, 2010, Nogueira *et al.*, 2013) which is what normally occurs in nature.

Peters and Venart (1999), observed that roughness decreases the front velocity and induces higher dilution in the head region. This is due either to the additional resistance at the bottom (which promotes an earlier transition to the viscous/buoyant flow regime) or to the decrease of the buoyant driving force which is induced by the entrainment of ambient fluid trapped into the roughness spacing. As rough beds induce higher bottom resistance and the buoyant driving force decreases due to enhanced entrainment of ambient fluid, increases in size and mass of the head are generally observed (Hallworth *et al.*, 1996, Peters and Venart, 1999). Moreover, large turbulence structures and billows are seen to be replaced by smaller structures so the current's head looks shorter and less well defined (Batt, 2008).

La Rocca *et al.* (2008) carried out experiments with instantaneous three-dimensional gravity currents flowing over a thin layer of particles (glued to the bed) ranging from 0.7 mm to 3.0 mm. The front velocity was seen to decrease with the increase of the mean diameter of the roughness elements. Although generally higher entrainment and dilution are associated with more rough beds, Nogueira *et al.* (2013)'s results do not confirm this trend for all the roughness sizes. Therefore, despite previous contributions, the effect of the bed roughness in the kinematics of gravity currents is far from being completely understood.

3. Experimental methods

Experiments were performed to assess both mass distribution and velocity fields of gravity currents (generated from a point and continuous release of dense fluid) propagating in confined geometries over different roughness beds. The use of a full-glass tank allows for the employment of Particle Image Velocimetry (PIV) and image analysis techniques from high-speed video recording. Both are used to measure different plan views of the phenomena, including profile and top views for two different regions (near and far from the discharge).

3.1. The set-up and instrumentation

All the experiments were carried out at the Hydraulics Laboratory of the Civil Engineering Department at Instituto Superior Técnico (IST) in the facility illustrated in Figure 3. This includes a tank (A) with outer dimensions $L \times W \times H$ of 3000×200×400 mm which is made from 12 mm thick glass panels, allowing for a clear visualization of the gravity current.

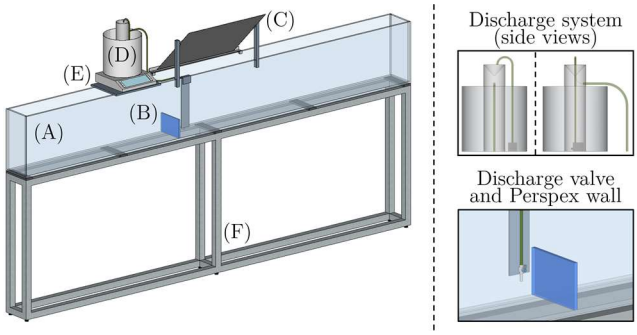

Figure 3 - Schematic overview of the facility and details on the discharge system.

Inside, a Perspex wall (B) is placed perpendicularly to the sidewalls, dividing the tank in two parts and providing the main geometry constraint; the gravity current develops along the largest side with an area of 1800×200 mm^2. Top view recordings are available by using a tilted mirror (C) that can be held above each field of view (FOV). The dense fluid discharge is performed from a supply tank (D) through an 8-mm diameter pipe. The overflow configuration of the recipient ensures a constant piezometric line being the flow started and stopped by a downstream valve right above the free surface. Although, the outlet is submerged in the ambient fluid, avoiding major free surface perturbations. The flow rate has been assessed from a scale (E) placed bellow the supply tank, registering the temporal variation of dense fluid's mass. As for the mirror, a LED panel can be placed below each FOV between the tank and the support structure (F).

The PIV system includes a high-power light source, in this case a Nd:YAG laser that emits an infrared light (wavelength of 1064 nm) which is then converted into a green light (wavelength of 532 nm) by a system of nonlinear optical materials. A camera from Dantec Dynamics© with a resolution of 1600×1200 px^2 is used for the image recording. The system includes also a computer with appropriate hardware and software (DynamicStudio) used for the synchronization during the acquisition and the later data treatment process. A complete description of a PIV typical setup and methodology can be found in Ferreira (2011).

The acquisition system used for the mass distribution measurements includes a high-speed camera AVT Bonito CL-400 with resolution set to 2320×750 px^2 and frame rate of 100 fps. The camera is connected to a custom-built computer and the software Norpix StreamPix6 enables the visualization, control and acquisition from the camera.

3.2. Experimental parameters

The mixture used in both calibration and experiments of the mass distribution technique is brine ($NaCl$ solution prepared from Kosher salt) dyed with Rhodamine WT® which has been used as tracer to visualize the gravity current. The particles of salt and rhodamine are herein called as contaminant. The

properties of the mixture are described in the Table 1 and the mean discharge, obtained with the scale measurements, as well as the other parameters and conditions are summarized in Table 2.

Table 1 - Details on the mixture preparation.

Freshwater density (g.cm^{-3})	0.999
Rhodamine WT® density (g.cm^{-3})	1.150
Contaminant/freshwater mass ratio (%)	4.72
Final density of the mixture (g.cm^{-3})	1.027
Final density of the salt (g.cm^{-3})	2.920
Final volume of the mixture (L)	50.1

Table 2 - Discharge characteristics.

Total mass flow rate (g.s^{-1})	7.55
Contaminant flow rate (g.s^{-1})	0.314
Freshwater flow rate (g.s^{-1})	7.236
Outlet diameter (mm)	8.0
Cross-section area (mm^2)	50.27
Dynamic viscosity (kg.(ms)$^{-1}$)	1.066×10^{-3}
Kinematic viscosity (m^2.s^{-1})	1.04×10^{-6}
Reynolds number (-)	1127

Concerning the bed roughness, three setups are tested. While the first consists of solely the tank's bottom glass panel (herein called as smooth bed), the two rough configurations result from the distribution of silica beads throughout the bottom. These particles have a mean diameter, D_m, of 3 mm and provide a quasi-transparent rough bed which is a key aspect for the application of the high-speed video techniques further described in this text. While one of the rough beds is formed by a single layer of beads (the so-called semi-rough bed), the second results from pilling and compacting three layers of them and it is herein named as multi-rough configuration. In both cases, the bed material was set uniformly all over the tank and particle movements or bed forms were not present for all the runs (see Figure 4). The average thickness, d_r, of these layers is illustrated in Figure 5.

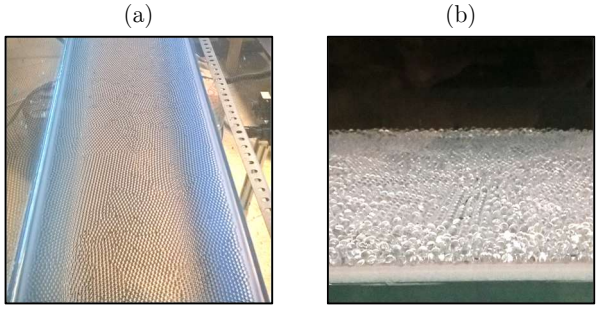

Figure 4 - The rough bed configurations: (a) semi-rough with a single layer and (b) multi-rough with three layers of particles.

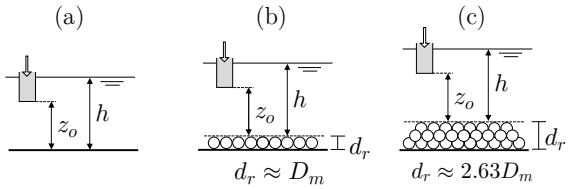

Figure 5 - Freshwater depth, h, and height of the outlet, z_o, for the (a) smooth, (b) semi-rough and (c) multi-rough beds.

The current propagation is analysed in two top view areas, near and far fields (see Figure 6), each with an area of about 600×200 mm^2 (a) or 250×200 mm^2 (b). PIV technique is also applied along the profiles shown in Figure 7.

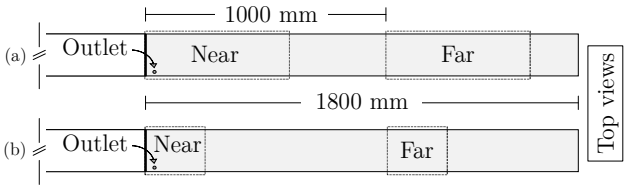

Figure 6 - Near and far fields for top view recordings with (a) high-speed video and (b) PIV technique.

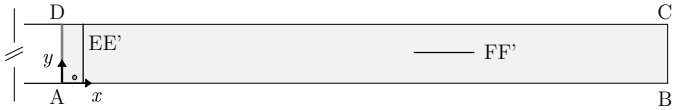

	Profile EE'	Profile FF'
Coordinates (cm)	$x = 5$	$100 < x < 118$
	$0 < y < 20$	$y = 9$

Figure 7 - Schematic location and referencing of the PIV profiles with identification of the tank's sidewalls.

3.3. The image analysis techniques

Mass distribution

The distribution of mass is obtained from a correlation with the light intensity in the recorded images. A pixel-by-pixel approach is applied since (1) the light emission from the LED panel is not completely homogeneous and (2) the conversion from light intensity to grey values might not be exactly the same for all the pixels. In the present study, the source of light is LED because it is a type of lighting that has reduced flickering, which has to be to minimized for the present photometric methodology.

The calibration, that precedes the experiment, comprises several runs in which the mass of contaminant is increased by adding a known volume of dense mixture (brine with Rhodamine WT®) and the consequent light attenuation (i.e., decrease of the grey value) is analysed. In each acquisition, the mixture is uniformly spread along the tank's bottom and around 1000 images are acquired after the fluid

could be considered fully steady inside the tank. The average grey tone is calculated for each run and is correlated with the known volume of contaminant.

Table 3 - Calibration of a pixel with the mass of contaminant being expressed in mg.cm^{-2} (a) and $\times 10^{-3}$ mg.px^{-2} (b) while the mean light intensity (c) is expressed in values of grey.

(a)	0	13.55	27.09	40.64	54.19	67.74	81.28	94.83
(b)	0	8.60	17.19	25.79	34.38	42.98	51.57	60.17
(c)	160.45	101.93	86.78	78.81	73.19	68.73	64.92	61.86

(a)	108.38	121.93	135.47	149.02	162.57	176.11	189.66	203.21
(b)	68.76	77.36	85.95	94.55	103.15	111.74	120.34	128.93
(c)	59.17	56.68	54.40	52.46	50.70	48.96	47.35	46.04

Then the mean grey values (G) are plotted against the known mass comprised in each pixel (M_c) in order to obtain the best fitting model. For this case the fitting function is given by:

$$M_c(G) = P_1(G - P_2)^{-P_3} - P_4 \qquad (2)$$

where the coefficients (P_i) are optimized by a nonlinear least-squares solver. The result of the example above is shown in Figure 8.

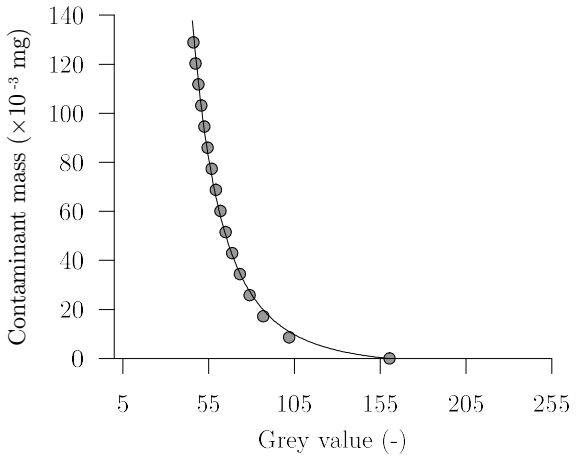

Figure 8 - Calibration points and curve-fitting for a single pixel.

Front detection

The detection of the current's front is performed through a technique that uses the raw images acquired for the mass distribution, being also based on the light attenuation caused by the dyed brine. As high-speed video is acquired at 100 fps, it is possible to have a good estimation of the quasi-instantaneous velocity of the front over the three different bed configurations. In order to obtain the position of the current the main steps performed are: (i) subtract each instant (frame) of the experiment to a baseline image (tank filled with freshwater only); (ii) apply a low-pass filter in which each pixel is compared to its "neighbours" and the spurious points in both white and black regions are corrected; (iii) convert all the images in matrixes of black and white values; (iv) find and register the set of coordinates x and y along the border of the current (i.e., black region). An example of a binary matrix converted from raw images and the matching output over the original image is shown in Figure 9.

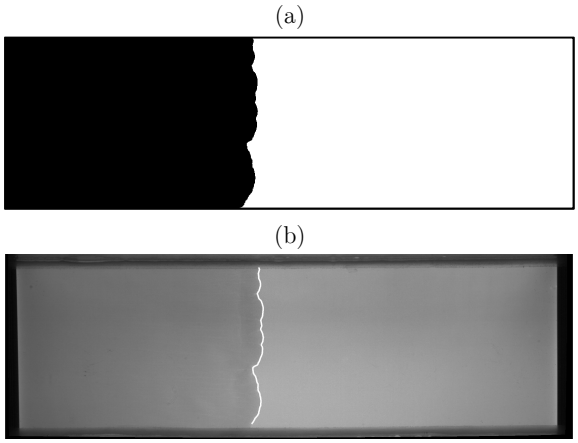

Figure 9 - Example of binary matrix (a) used in the detection of the current's front (b).

Depth of the current

In the present work, the current's depth is determined from the far-field profile view of the flow which is acquired with the PIV technique. That being said, since tracer particles are added solely to the dense fluid that produces the gravity current, a new methodology for the definition of its depth is proposed; it consists of evaluating the upper boundary of the current as the lowest limit above which there is only ambient fluid and below which seeding particles can still be observed. PIV acquisition leads to raw images where the contrast between the seeding particles and all the other elements is high, i.e. the seeding is typically represented by bright points over a dark background. The depth of the current is assumed to be the distance between the bottom and the upper limit defined in the beginning of this section. While the former is taken as a straight line, the latter must follow the depth variation that is observed along the current (especially in the frontal zone). A statistic method is applied to define an outline over the density current, eliminating the spurious values that are either in the ambient fluid or too deep in the inner region of the current.

4. Results

4.1. Flow visualization in the near field

Initial propagation

Once the discharge starts, it is noticeable that the current does not propagate in a perfect radial pattern before travelling the full width of the tank. This asymmetry is illustrated in Figure 10 where the white line matches the front and the detection limit concentric to the outlet. This flow configuration is due to the fact that the outlet is not equally distant from the confining walls (25 mm from wall AB and 35 mm from AD – see Figure 7 for referencing).

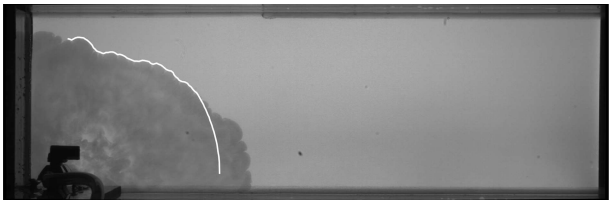

Figure 10 - Sample of the front detection in the near field for $t = 7.2$ s after the beginning of the discharge.

As depicted in Figure 12, 8 s after the beginning of the discharge, the current reaches the sidewall CD and the accumulation of mass starts. Due to the transfer of momentum from the horizontal to the vertical direction, the brine runs up the sidewall and the local depth increases ($t = 12$ s). This can be observed in the PIV acquisition shown in Figure 11 (profile EE').

Figure 11 - PIV acquisition along the profile EE'.

Meanwhile, dense fluid keeps flowing towards the wall and the accumulation zone becomes larger. At this point, the pressure gradient cannot be sustained for longer and the elevated fluid generates a wave ($t = 14$ s) that is probably a combination between a purely non-linear wave – which would generate a shock – and a non-linear-dispersive wave – a soliton.

Since the reflected wave is formed in the sidewall CD and it travels at a higher velocity than the current's front, they successively merge from the left to the right side, i.e. from the top to the bottom in the maps of Figure 12. During this process, two main effects can be observed: an increase in the front's propagation velocity and an accumulation of mass in the head region. The first can be observed between $t = 18$ s and $t = 23$ s, as the left side of the front overtakes the right side. In turn, the second effect is depicted in the highlighted head (meaning higher contaminant mass values) which is noticeable for $t = 23$ s. Nonetheless, the constant entrainment of freshwater causes the dilution of this accumulation and the highlighted region vanishes after about 3.5 s (for $t = 27.5$ s).

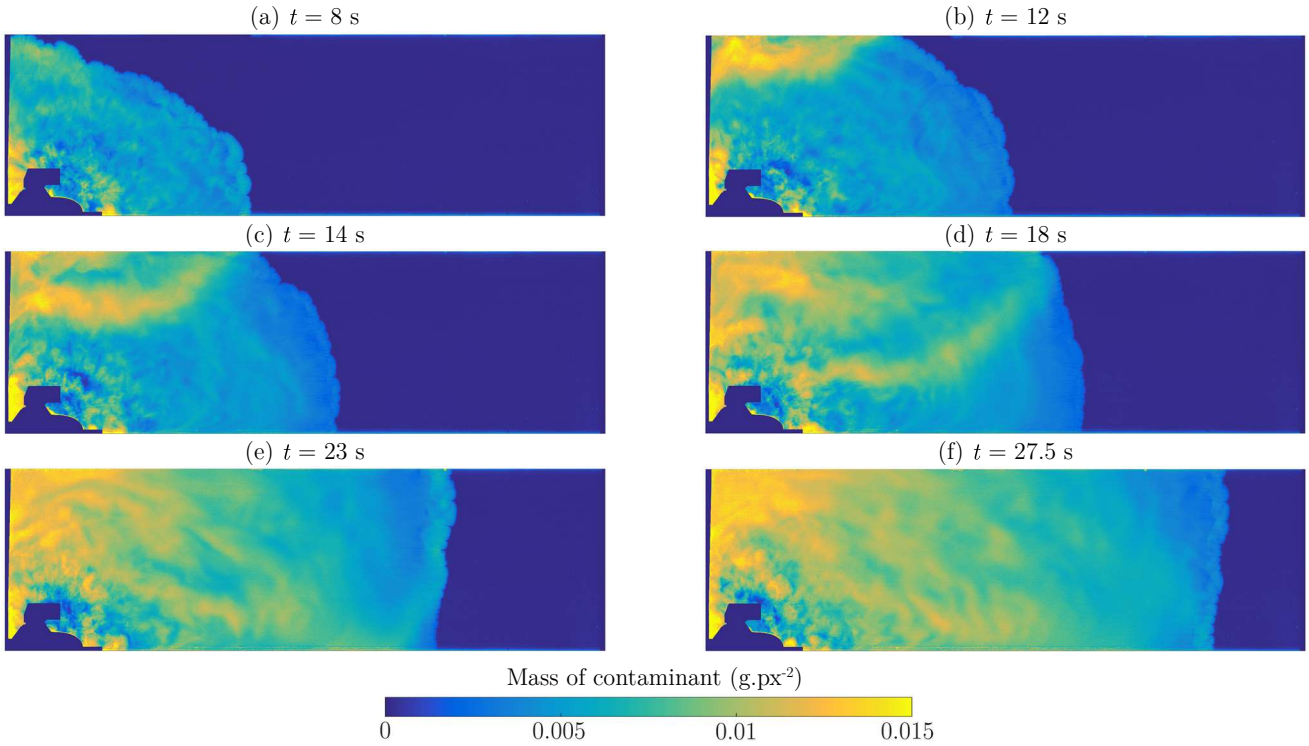

Figure 12 - Contaminant mass distribution in the near field t seconds after the discharge.

Effects on the front structures

The front detection algorithm was used in the region where the merging of the reflected wave and the current's front occurs. The plots shown in Figure 13 represent the time distribution (xx axis) of the quasi-instantaneous velocity along the width of the tank (yy axis). The first feature to be noticed is the earlier detection along the right sidewall. During these first instants, diagonal darker strings can be observed rising from the most forward positions (i.e., the first to be detected) which correspond to the lobes formation. These lines extent for some seconds suggesting a continual higher local velocity that can be interpreted as a growing lobe. They essentially develop in the direction of the most backward positions which is also in accordance with the previous hypothesis since the lobe can develop laterally if it is not constrained by another one. That being said, this type of instability (lobes and clefts) is more pronounced as more rough is the bed.

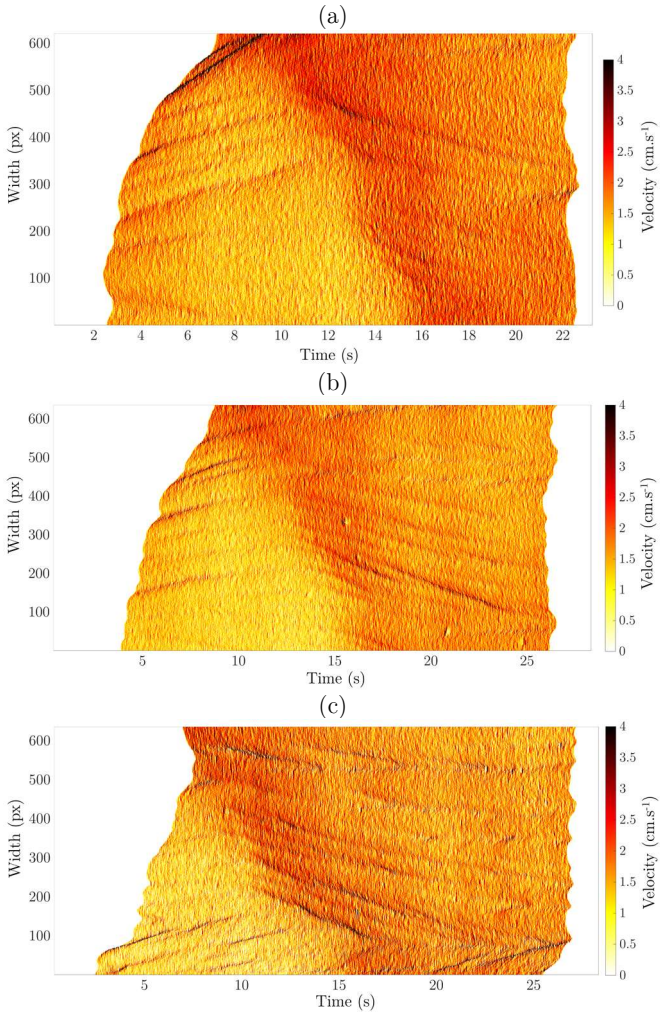

Figure 13 - Time-width distribution of the quasi-instantaneous velocities of the front in the near field for the (a) smooth, (b) semi-rough and (c) multi-rough beds.

The reflected wave does not merge simultaneously with the whole front. Hence, the effect on the velocity is represented by the oblique shadowed zone which can be observed in all the plots of Figure 13. When the two entities merge, there is a clear transfer of momentum from the reflected wave to the structures at the front of the current which is denoted in the alignment of the dark strings' pattern with the propagation direction of the reflected wave.

Effects on the body of the current

As the current's front advances (leaving the near field) the contaminant mass increases all over the maps as it is depicted in Figure 14.

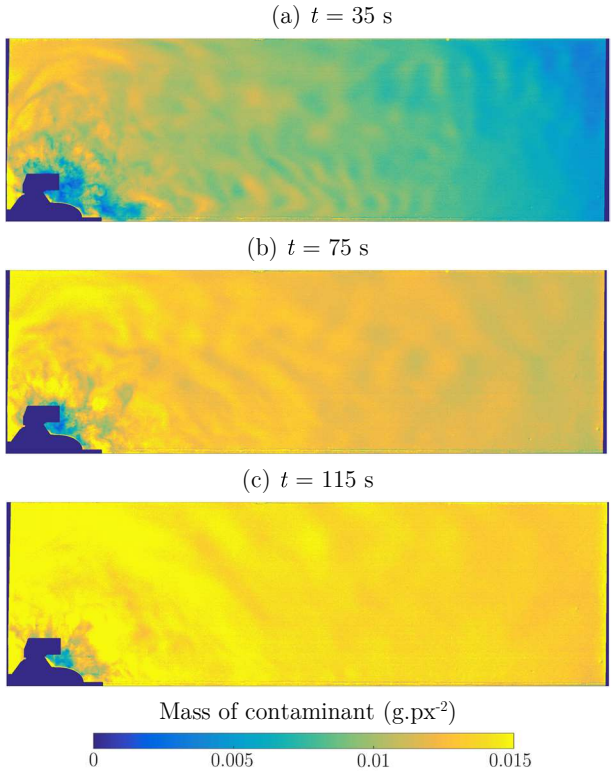

Figure 14 - Contaminant mass distribution in the near field t seconds after the discharge.

Moreover, the contaminant accumulation is particularly enhanced in the vicinity of the corner ADC where the entrainment of ambient fluid is attenuated by the presence of the recirculation cell that is formed in that zone (Figure 15).

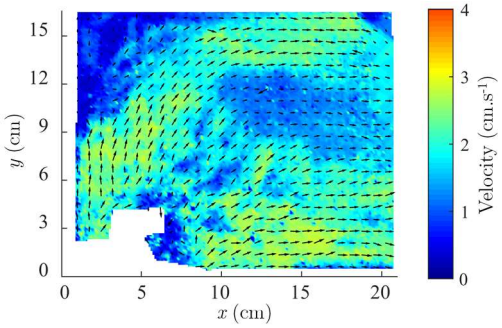

Figure 15 - Velocity field in the near field ($t = 30$ s).

4.2. Flow visualization in the far field

The behaviour of the front

When the current flows from the near to the far field, the shape of the front becomes more linear, propagating perpendicularly to the sidewalls of the tank. As seen before, part of this uniformization process is induced by the reflections that end up at the front, causing local accelerations that interfere with the structure of the lobes and clefts. The front's mean velocity for each type of bed are shown in Figure 16 (t_0 marks the beginning of the detection for x = 100 cm).

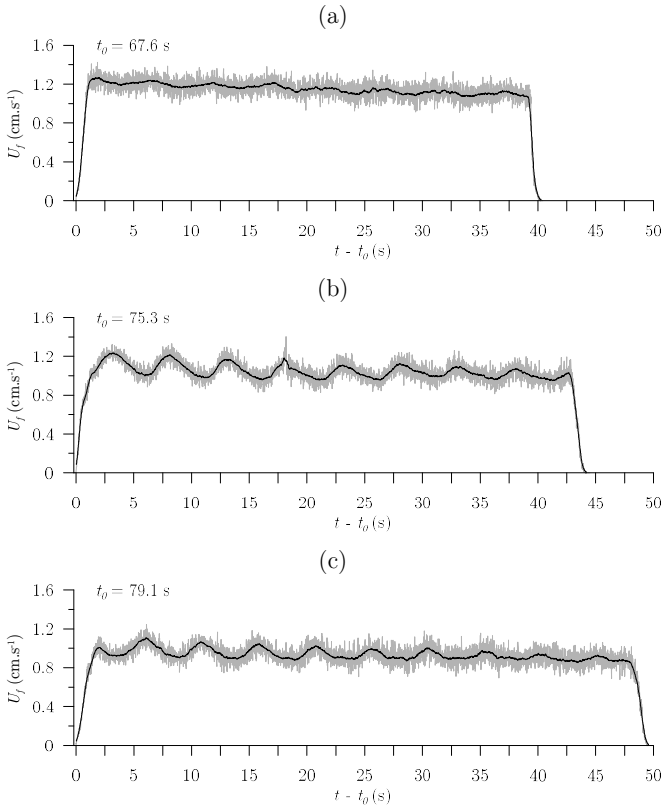

Figure 16 - Mean velocity of the front, U_f, for the (a) smooth, (b) semi-rough and (c) multi-rough beds (with moving average).

As depicted in the previous plots, the highest values are observed for the smooth configuration (U_f = 1.118 cm.s^{-1}), followed by the semi-rough (U_f = 1.019 cm.s^{-1}) and multi-rough (U_f = 0.908 cm.s^{-1}) beds. These results are in accordance with the observations of Peters and Venart (1999), Batt (2008) and La Rocca *et al.* (2008) for which a decrease on the front velocity is observed in the presence of rough surfaces. However, attention is given to the low-frequency oscillations which are not mentioned in any of those works. Despite the noise of the signals, these oscillations are observed for all three plots with emphasis on the rough configurations.

Since the temporal resolution of the data is constant, these velocity oscillations are caused by differences in the distance travelled by the front's centre of mass which in turn might be due to two reasons: (1) the lobes and clefts formation and (2) the propagation of the reflections occurring in the near field. Assuming the first hypothesis, during the formation of a cleft, the front is detected in a backward position relatively to the rest of the current's front, thus contributing to a delay of the mean advancing ratio. By contrast, when two clefts merge, that contribution is reduced and a higher mean velocity is detected. Concerning the second hypothesis, the velocity fluctuations might result from the arrival of reflections at the current's front as it has been shown in the near field. In that scenario, the reflected waves mainly propagate in a non-parallel path with respect to the sidewalls of the tank due to the asymmetrical configuration of the experiments. Hence, their arrival at the far field is expected to result from a sloshing-like effect, i.e. after multiple reflections on the sidewalls. Taking into account the plots of the Figure 13, these waves would not arrive parallel to the current's front and local increases on the front's velocity would be registered sequentially along the width of the channel. The time-width distribution of the quasi-instantaneous velocities of the front for each bed is presented in Figure 17.

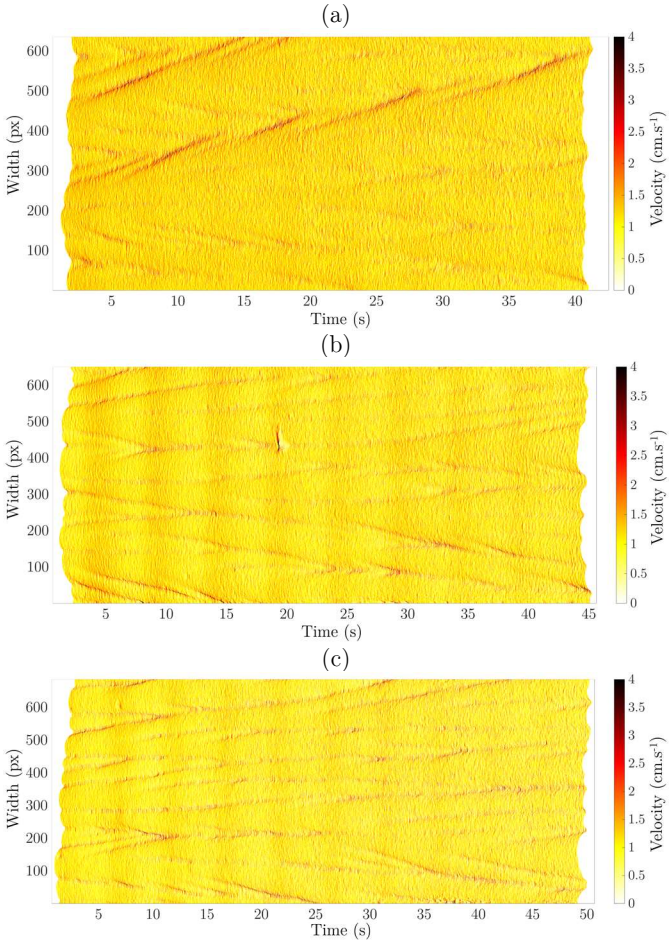

Figure 17 - Time-width distribution of the quasi-instantaneous velocities of the front in the far field for the (a) smooth, (b) semi-rough and (c) multi-rough beds.

Once again, the darker strings in these plots seem to be related with the lobes and clefts formation. Actually, despite the plots represent quasi-instantaneous velocities, the pattern in the semi and multi-rough configurations resemble the drawings from Simpson (1972) for the time-evolution of lobes. Moreover, the observations of Batt (2008) regarding the effects of bed roughness on the size of the turbulence structures and billows appear to be replicated in the plots above as the pattern of the multi-rough configuration looks more fragmented than in the semi-rough.

The structure of the current's body

When the current travels the full length of the tank, a new reflection occurs in the end wall. As shown before, at this point, the flow can be considered unidimensional and the impact occurs along the normal to this wall. In light of this, the present section draws attention to the evolution of the current's depth and the structure of the velocity field, resulting both data from the PIV profile recorded along the mid-with section in the far field. The evolution of the current's depth for the three bed configurations is shown in Figure 18.

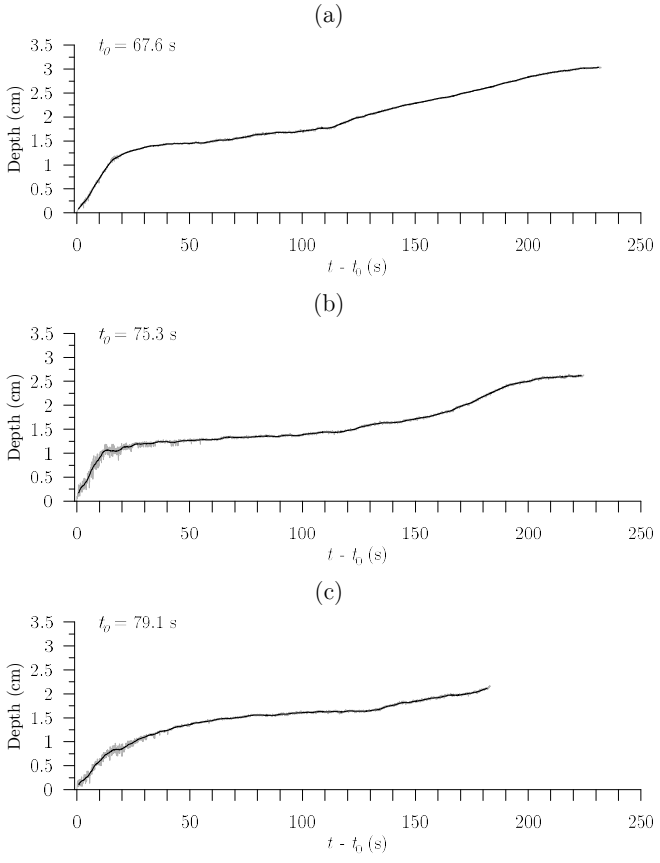

Figure 18 - Current depth evolution for the (a) smooth, (b) semi-rough and (c) multi-rough bed configurations (black line represents the moving average).

Looking at the first instants of detection, as the current starts to fill the width of the image, the depth evolution is marked by a steep increase during 15-20 seconds. From that point, the increasing rate is significantly lower, allowing for an estimation of the current's depth evolution in the body region. Although the transition happens in the three experiments, it is smoother for the multi-rough configuration. This result suggests that dense fluid gradually fills the voids between the beads on the bed, leading to a slower increase of the depth. Also, the resistance induced by the bottom roughness should lead to a higher depth which is not evident, namely for the semi-rough configuration. Once again, it might be explained by the entrainment of dense fluid in the bed since the depth is measured from the top of the bed crests.

Regarding the inner structure of the current, the velocity fields during the reflection on the end wall of the tank are shown in Figure 19. Before the current arrives at the end wall, a quasi-steady velocity field can be observed ($t - t_0 = 64$ s). Then, the effect of the impact starts to propagate upstream in the form of a region of lower velocities that expands from the left side on the velocity fields ($t - t_0 = 118$ s) along the full depth of the current. This is also reflected in the increase of the current's depth which is visible in the plots of Figure 18 as an inflection point that occurs at about $t - t_0 = 110$ s (smooth), $t - t_0 = 115$ s (semi-rough) and $t - t_0 = 135$ s (multi-rough). At a given instant, a backflow can be observed entering the field of view which occurs for $t - t_0 = 170$ s (smooth), $t - t_0 = 170$ s (semi-rough) and $t - t_0 = 180$ s (multi-rough). From this point, two layers flowing in opposite directions can be distinguished in the gravity current and the continuous replenishment of dense fluid forces the layer underneath to accelerate again.

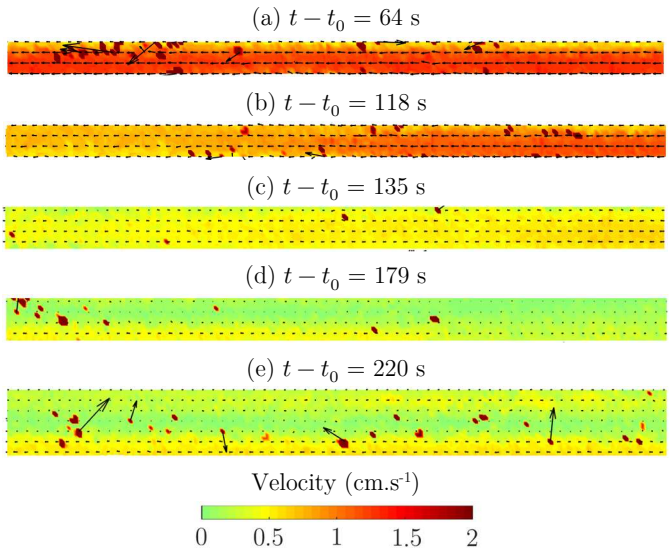

Figure 19 - Velocity fields of the current propagating in the far field (smooth bed experiments).

5. Conclusions

The present work intended to observe gravity currents in which the driving force is beyond the simple density gradient, i.e. currents that are subjected to the effects that arise from the interactions with the bottom roughness and the rigid boundaries. Laboratory experiments revealed that typical structures characterizing these flows are affected by reflected waves, namely during the first moments when the resistance at the bottom does not play such an important role. The mass distribution analysis suggests that those reflections are responsible for a transfer of mass to the front of the current which in turn lead to local accelerations. The same technique also allowed for the identification of regions of lower dilution. These latter appear as a consequence of the recirculation structures that could be observed in the flow velocity fields.

When the current propagates to the far field, there is a loss of momentum that is not only due to the bottom resistance, but also to dense fluid that flows through the voids in the rough beds and inhibits the depth increase that would provide the driving force. The decrease of the front's velocity for the rough configurations is in accordance with previous studies. However, the tracking methodology revealed oscillations that have not been mentioned in the past and which might be related to the reflections from the near field.

References

Batt, R. L. (2008), The influence of bed roughness on the dynamics of gravity currents, PhD Thesis. University of Leeds.

Buckee, C., Kneller, B. and Peakall, J. (2001). "Turbulence structure in steady, solute-driven gravity currents." *Particulate gravity currents*, 173-187.

Cenedese, C. and Adduce, C. (2010). "A new parameterization for entrainment in overflows." *Journal of Physical Oceanography*, 40 (8), 1835-1850.

Cesare, G. D., Schleiss, A. and Hermann, F. (2001). "Impact of turbidity currents on reservoir sedimentation." *Journal of Hydraulic Engineering*, 127 (1), 6-16.

Doronzo, D. M., Martí, J., Dellino, P., Giordano, G. and Sulpizio, R. (2016). "Dust storms, volcanic ash hurricanes, and turbidity currents: physical similarities and differences with emphasis on flow temperature." *Arabian Journal of Geosciences*, 9 (4), 1-9.

Ellison, T. H. and Turner, J. S. (1959). "Turbulent entrainment in stratified flows." *Journal of Fluid Mechanics*, 6 (03), 423-448.

Hallworth, M. A., Huppert, H. E., Phillips, J. C. and Sparks, R. S. J. (1996). "Entrainment into two-dimensional and axisymmetric turbulent gravity currents." *Journal of Fluid Mechanics*, 308 289-311.

Kneller, B. and Buckee, C. (2000). "The structure and fluid mechanics of turbidity currents: a review of some recent studies and their geological implications." *Sedimentology*, 47 (s1), 62-94.

La Rocca, M., Adduce, C., Sciortino, G. and Pinzon, A. B. (2008). "Experimental and numerical simulation of three-dimensional gravity currents on smooth and rough bottom." *Physics of Fluids*, 20 (10), 106603.

Martin, J. E. and García, M. H. (2009). "Combined PIV/PLIF measurements of a steady density current front." *Experiments in Fluids*, 46 (2), 265-276.

Morozov, E. G., Trulsen, K., Velarde, M. G. and Vlasenko, V. I. (2002). "Internal tides in the Strait of Gibraltar." *Journal of Physical Oceanography*, 32 (11), 3193-3206.

Nogueira, H. I. S., Adduce, C., Alves, E. and Franca, M. J. (2013). "Analysis of lock-exchange gravity currents over smooth and rough beds." *Journal of Hydraulic Research*, 51 (4), 417-431.

Oehy, C. D. and Schleiss, A. J. (2007). "Control of turbidity currents in reservoirs by solid and permeable obstacles." *Journal of Hydraulic Engineering*, 133 (6), 637-648.

Parker, G., Garcia, M., Fukushima, Y. and Yu, W. (1987). "Experiments on turbidity currents over an erodible bed." *Journal of Hydraulic Research*, 25 (1), 123-147.

Peters, W. D. and Venart, J. E. S. (1999), Rough-surface gravity current flows, Thesis. University of New Brunswick, Department of Mechanical Engineering.

Sequeiros, O. E., Spinewine, B., Beaubouef, R. T., Sun, T., García, M. H. and Parker, G. (2010). "Characteristics of velocity and excess density profiles of saline underflows and turbidity currents flowing over a mobile bed." *Journal of Hydraulic Engineering*, 136 (7), 412-433.

Shin, J. O., Dalziel, S. B. and Linden, P. F. (2004). "Gravity currents produced by lock exchange." *Journal of Fluid Mechanics*, 521 1-34.

Simpson, J. E. (1969). "A comparison between laboratory and atmospheric density currents." *Quarterly Journal of the Royal Meteorological Society*, 95 (406), 758-765.

Simpson, J. E. (1972). "Effects of the lower boundary on the head of a gravity current." *Journal of Fluid Mechanics*, 53 (04), 759-768.

Simpson, J. E. (1982). "Gravity Currents in the Laboratory, Atmosphere, and Ocean." *Annual Review of Fluid Mechanics*, 14 (1), 213-234.

Simpson, J. E. (1997). *Gravity currents: In the environment and the laboratory*. Cambridge University Press.

Stacey, M. W. and Bowen, A. J. (1988). "The vertical structure of density and turbidity currents: theory and observations." *Journal of Geophysical Research: Oceans*, 93 (C4), 3528-3542.

Stagnaro, M. and Pittaluga, M. B. (2014). "Velocity and concentration profiles of saline and turbidity currents flowing in a straight channel under quasi-uniform conditions." *Earth Surface Dynamics*, 2 (1), 167.

Theiler, Q. and Franca, M. J. (2016). "Contained density currents with high volume of release." *Sedimentology*, 63 (6), 1820-1842.